Blind Haze Separation

Sarit Shwartz , Einav Namer and Yoav Y. Schechner

Dept. of Electrical Engineering
Technion - Israel Inst. Technology
Haifa 32000, ISRAEL
psarit@tx.technion.ac.il,{einav,yoav}@ee.technion.ac.il

Abstract

Outdoor imaging is plagued by poor visibility conditions due to atmospheric scattering, particularly in haze. A major problem is spatially-varying reduction of contrast by stray radiance (airlight), which is scattered by the haze particles towards the camera. Recent computer vision methods have shown that images can be compensated for haze, and even yield a depth map of the scene. A key step in such a scene recovery is subtraction of the airlight. In particular, this can be achieved by analyzing polarization-filtered images. However, the recovery requires parameters of the airlight. These parameters were estimated in past studies by measuring pixels in sky areas. This paper derives an approach for blindly recovering the parameter needed for separating the airlight from the measurements, thus recovering contrast, with neither user interaction nor existence of the sky in the frame. This eases the interaction and conditions needed for image dehazing, which also requires compensation for attenuation. The approach has proved successful in experiments, some of which are shown here.

1 Stray Radiation in Haze

Imaging in poor atmospheric conditions [3, 7, 12, 20] affects human activities, as well as remote sensing and surveillance. Hence, analysis of images taken in haze is important. Moreover, research into atmospheric imaging promotes other domains of vision through scattering media, such as water [9, 11, 14, 23, 24, 31] and tissue. Several methods have been proposed to restore good visibility [9, 11, 14, 30] in such media. An effective approach for analyzing hazy images is based on polarization [17, 25]. It capitalizes on the fact that one of the sources of image degradation in haze is partially polarized. Such analysis yields the scene's distance map, in addition to a dehazed image.

Haze parameters are required to invert the effects of haze. In particular, it is important to know the parameters of stray light (called airlight [17]) created by haze, which greatly decreases image contrast. These parameters can be determined from the image data itself. This was shown by [18] in cases of fog or heavy haze (achromatic scattering), in a method requiring inter-frame weather changes,
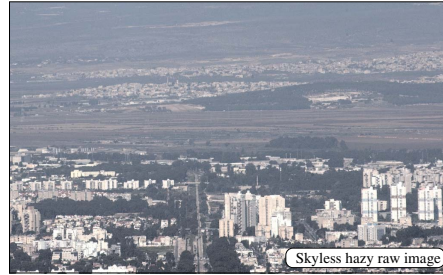

Figure 1. Raw hazy image. Recovering contrast requires haze parameters. Had the sky existed in the FOV, these parameters could have been measured directly from the image. This however, is not the case in the above scene.

i.e., long acquisition periods. In contrast, we focus on the polarization-based approach, since its image acquisition is fast, and thus practical.[1] In this approach, the required parameters have been derived [25] from measurements of pixels that correspond to *sky* by the *horizon* (even automatically [17]). Thus, this parameter estimation relies on the existence of such an image part in the field of view (FOV).

This work proposes a method that addresses this problem. The method *blindly* separates the airlight radiance (the main cause for contrast degradation) from the object's signal. It works even if no sky exists in the FOV, as in the scene shown in Fig. 1. The parameter that determines this separation is estimated without any user interaction. The method exploits mathematical tools developed in the field of blind source separation (BSS), also known as independent component analysis (ICA). This field has already contributed to solving image separation [6, 21, 26, 27, 28, 32] problems,[2] particularly with regard to reflections. The problem of haze is more complex than reflections, since object recovery is obtained by nonlinear interaction of the raw images. Moreover, the assumption of independence upon which ICA relies is not trivial to accommodate, as we later explain. Nevertheless, we show that the radiance of haze (airlight) can be separated by ICA, by the use of a simple pre-process. We note that dehazing was attempted by using ICA based on color cues [19]. However, an implicit underlying assump-

---

[1] Polarization aids other computer vision aspects [4, 16, 26, 34].
[2] ICA has also been used in high-level vision [5, 13, 33].

tion behind Ref. [19] is that the radiance is identical to all the color channels, i.e. the scene is gray. This is untypical in nature.

We emphasize that our method is *physics-based*, rather than being pure ICA of mathematically abstract signals. Thanks to this approach to the problem, common ICA ambiguities are avoided. This separation step reduces the user interaction needed for dehazing. We successfully applied this method in several real experiments conducted in haze. We obtained blind parameter estimation which was consistent with direct sky measurements. Consequently, dehazing showed significant improvement of visibility and color, relative to the raw data.

2   Theoretical Background

To make the paper self-contained, this section briefly reviews the known formation model of hazy images. It also describes a known inversion process of this model, which recovers good visibility. This description is based on Ref. [25]. An acquired frame is a combination of two main components. The first originated from the object radiance. Let us denote by L^{object} the object radiance as if it was taken in a clear atmosphere, without scattering in the line of sight. Due to attenuation in the haze, the camera senses a fraction of this radiance.[3] This attenuated signal is the *direct transmission*

$$D = L^{\mathrm{object}} t , \qquad (1)$$

where
$$t = e^{-\beta z} \qquad (2)$$

is the transmittance of the atmosphere. The transmittance depends on the distance z between the object and the camera, and on the atmospheric attenuation coefficient β.

The second component is known as *path radiance*, or *airlight*. It originates from the scene illumination (e.g., sunlight), a portion of which is scattered into the line of sight by the haze. It is given by

$$A = A_\infty (1 - t) . \qquad (3)$$

Here A_∞ is the value of airlight at a non-occluded horizon. It depends on the haze and illumination conditions. Contrary to the direct transmission, airlight increases with the distance and dominates the acquired image irradiance

$$I^{\mathrm{total}} = D + A \qquad (4)$$

at long range. The addition of airlight is a major cause for reduction of signal contrast.

In haze, the airlight is often partially polarized. Hence, the airlight image component can be modulated by a

---

[3]There is a proportion between the scene radiance and image irradiance. We treat them as equivalent, since this proportionality depends on the imaging system, not on the atmosphere.

mounted polarizer. At one polarizer orientation the airlight contribution is least intense. Since the airlight disturbance is minimal here, this is the *best state* of the polarizer. Denote this airlight component as A^{min}. There is another polarizer orientation (perpendicular to the former), for which the airlight contribution is the strongest, and denoted as A^{max}. The overall airlight given in (Eq. 3) is given by

$$A = A^{\mathrm{min}} + A^{\mathrm{max}} . \qquad (5)$$

Assuming that the direct transmission is not polarized, the energy of D is equally split among the two polarizer states. Hence, the overall measured intensities at the polarizer orientations mentioned above are

$$I^{\mathrm{min}} = A^{\mathrm{min}} + D/2 \quad , \quad I^{\mathrm{max}} = A^{\mathrm{max}} + D/2 \quad . \quad (6)$$

The degree of polarization (DOP) of the airlight is defined as

$$p = (A^{\mathrm{max}} - A^{\mathrm{min}})/A , \qquad (7)$$

where A is given in Eq. (3). For narrow FOVs, this parameter does not vary much. In this work we assume the value of this parameter to be spatially constant. Note that

$$0 \le p \le 1 . \qquad (8)$$

It follows that

$$I^{\mathrm{min}} = A(1-p)/2 + D/2 \quad , \quad I^{\mathrm{max}} = A(1+p)/2 + D/2. \qquad (9)$$

It is easy to see from (4,9), that $\hat{I}^{\mathrm{total}} = I^{\mathrm{min}} + I^{\mathrm{max}}$.

Dehazing is performed by inverting the image formation process. The first step separates the haze radiance (airlight) A from the object's direct transmission D. The airlight is estimated as

$$\hat{A} = (I^{\mathrm{max}} - I^{\mathrm{min}})/p . \qquad (10)$$

Then, Eq. (4) is inverted to estimate D. Subsequently, Eq. (1) is inverted based on an estimate of the transmittance (following Eq. 3)

$$\hat{t} = 1 - \hat{A}/A_\infty . \qquad (11)$$

These operations are compounded to dehazing

$$\hat{L}^{\mathrm{object}} = (I^{\mathrm{total}} - \hat{A})/\hat{t} . \qquad (12)$$

Two problems exist in this process. First, the estimation (i.e., separation) of airlight requires the parameter p. Secondly, compensation for attenuation requires the parameter A_∞. Both of these parameters are generally unknown, and thus provide the incentive for this paper. In the past, these parameters were estimated based on pixels which correspond to the sky near the horizon. However, in general, "sky" pixels may not always be available in the FOV. Moreover, the sky by the horizon may be cloudy, ruining this kind of estimation.

3 Blind Estimation of p

In this section, we develop a method for blindly estimating p based on low-level computer vision. It results in blind separation of A from D. First, note that Eq. (12) can be rewritten as

$$\hat{L}^{\text{object}} = \frac{(1-1/p)I^{\max}(x,y) + (1+1/p)I^{\min}(x,y)}{1 - [I^{\max}(x,y) - I^{\min}(x,y)]/(A_{\infty}p)} \ . \tag{13}$$

This is a nonlinear function of the raw images $I^{\max}$ and $I^{\min}$, since they appear in the denominator, rather than just superimposing in the numerator. This nonlinear interaction makes it difficult to tap onto the vast tools that have been developed in the ICA field for linear separation problems.

3.1 Facilitating Linear ICA

To facilitate linear ICA, we look at a linear part of the model. This part attempts to separate the radiance $A(x,y)$ from $D(x,y)$, which is the attenuated signal of the object. As seen in Eq. (4), this coupling is linear. However, there is still a problem: as we detail in this section, the assumption of independence, upon which ICA relies, is questionable in this formulation. Thus, we describe a transformation that enhances the reliability of this assumption.

From Eq. (9), the two acquired images constitute the following equation system:

$$\begin{bmatrix} I^{\max} \\ I^{\min} \end{bmatrix} = \mathbf{M} \begin{bmatrix} A \\ D \end{bmatrix} , \tag{14}$$

where

$$\mathbf{M} = \begin{bmatrix} (1+p)/2 & 1/2 \\ (1-p)/2 & 1/2 \end{bmatrix} . \tag{15}$$

Thus, the estimated components are

$$\begin{bmatrix} \hat{A} \\ \hat{D} \end{bmatrix} = \mathbf{W} \begin{bmatrix} I^{\max} \\ I^{\min} \end{bmatrix} , \tag{16}$$

where

$$\mathbf{W} = \begin{bmatrix} 1/p & -1/p \\ (p-1)/p & (p+1)/p \end{bmatrix} . \tag{17}$$

Eqs. (14,16) are in the form used by linear ICA. Since p is unknown, then the mixing matrix $\mathbf{M}$ and separation matrix $\mathbf{W}$ are unknown. The goal of ICA in this context is: given only the acquired images $I^{\max}$ and $I^{\min}$, find the separation matrix $\mathbf{W}$ that yields "good" $\hat{A}$ and $\hat{D}$. For this purpose, a quality criterion must be defined and optimized. Typically, ICA would seek $\hat{A}$ and $\hat{D}$ that are statistical independent (see [8] and references therein). Thus, ICA assumes independence of A and D. However, this is a wrong assumption. The airlight A always increases with the distance z, while the direct transmission D decays, in general,
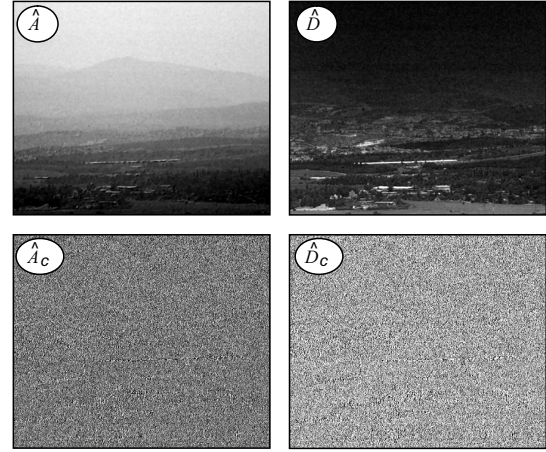

Figure 2. [Top] The direct transmission image $\hat{D}$ is strongly negatively correlated to the airlight $\hat{A}$. A wavelet channel of these images [Bottom] makes them much less mutually dependent.

with z (see Fig. 2). Thus, there is a strong negative correlation between A and D. There are local exceptions to this observations, in places where the inherent object radiance L^{object} increases with z. Nevertheless, due to this global correlation, A and D are highly mutually dependent. Therefore, how can we use ICA in this domain?

Fortunately, this statistical dependence does not occur in all image components. In fact, the high correlation mentioned above occurs in *very low* spatial frequency components: D decays with the distance only *roughly*. As noted, local behavior does not necessarily comply with this rough trend. Thus, in some image components (not low frequencies), we can expect significant independence (Fig. 2).

Hence, ICA can work in our case, if we transform the images to a representation that is more appropriate than raw pixels. We work only with linear transformations, since we wish to maintain the linear relations expressed in Eqs. (14)-(17). There are several common possibilities for linear operations that result in elimination of low frequencies. We opted for a wavelet transformation (see for example [29]), but the derivation is not limited to that domain. Define

$$D_c(x,y) = \mathcal{W}\{D(x,y)\} \tag{18}$$

as the wavelet (or sub-band) image representation of D. Here c denotes the sub-band channel, while $\mathcal{W}$ denotes the linear transforming operator. Similarly, define the transformed version of $A, \hat{A}, \hat{D}, I^{\max}$ and $I^{\min}$ as $A_c, \hat{A}_c, \hat{D}_c, I_c^{\max}$ and $I_c^{\min}$, respectively (see example in Fig. 2). Due to the commutativity of linear operations[4],

$$\begin{bmatrix} \hat{A}_c \\ \hat{D}_c \end{bmatrix} = \mathbf{W} \begin{bmatrix} I_c^{\max} \\ I_c^{\min} \end{bmatrix} , \tag{19}$$

---

[4]This commutativity has been exploited in ICA methods applied in other applications. See [10] and references therein.

where $\mathbf{W}$ is the same as defined in Eq. (17).

We now perform ICA over Eq. (19). As we shall see in the experiments, this approach works! Hence, the assumption of statistical independence in sub-band images is powerful enough to blindly deliver the solution. In our case, the solution of interest is the matrix $\mathbf{W}$, from which we derive p. Based on p, the airlight is estimated, and can then be separated from $D(x, y)$, as described in Sec. 2.

3.2 Scale Insensitivity

When attempting ICA, we should consider its fundamental ambiguities [8, 28]. One of them is *scale*: if two signals are independent, then they remain independent even if we change the scale of any of them (or both). Thus, ICA does not reveal the true scale[5] of the independent components. This phenomenon can be considered both as a problem, and as a helpful feature. The problem is that estimated signals may be ambiguous. However, in our case, we have a *physical model* behind the mixture formulation. As we shall see, this model eventually disambiguates the derived estimation. Moreover, we *benefit* from this scale-insensitivity. As we show in Sec. 3.3, the fact that ICA is insensitive to scale simplifies the intermediate mathematical steps we take.[6]

3.3 Optimization Criterion

Statistical dependency can be measured by mutual information (MI). The MI of $\hat{A}_c$ and $\hat{D}_c$ can be expressed as (see for example [2])

$$\mathcal{I}(\hat{A}_c, \hat{D}_c) = \mathcal{H}_{\hat{A}_c} + \mathcal{H}_{\hat{D}_c} - \mathcal{H}_{\hat{A}_c, \hat{D}_c} \ . \qquad (20)$$

Here $\mathcal{H}_{\hat{A}_c}$ and $\mathcal{H}_{\hat{D}_c}$ are the marginal entropies of $\hat{A}_c$ and $\hat{D}_c$, respectively, while $\mathcal{H}_{\hat{A}_c, \hat{D}_c}$ is their joint entropy. Let us look at the separation matrix $\mathbf{W}$ (Eq. 17). Its structure implies that up to a scale p, the estimated airlight $\hat{A}$ is a simple difference of the two acquired images. Denote $\tilde{A}_c$ as an estimation for the airlight component $\hat{A}_c$, up to this scale

$$\tilde{A}_c = I_c^{\max} - I_c^{\min} \ . \qquad (21)$$

Similarly, denote

$$\tilde{D}_c = w_1 I_c^{\max} + w_2 I_c^{\min} \qquad (22)$$

as the estimation of $\hat{D}_c$ up to a scale p, where

$$w_1 \equiv (p-1) \quad , \quad w_2 \equiv (p+1) \ . \qquad (23)$$

---

[5]A special case of scale ambiguity is the *sign* ambiguity, for which the scale is -1.

[6]An additional ICA ambiguity is *permutation*, which refers to mutual ordering of sources. This ambiguity does not concern us at all. The reason is that our physics-based formulation dictates a a special form for the matrix $\mathbf{W}$, and thus its rows are not mutually interchangeable.

Hence, the separation matrix of $\hat{D}_c$ and $\hat{A}_c$ is

$$\tilde{\mathbf{W}} = \begin{bmatrix} 1 & -1 \\ w_1 & w_2 \end{bmatrix} \ . \qquad (24)$$

Minimizing the statistical dependency of $\hat{A}_c$ and $\hat{D}_c$ means that $\tilde{A}_c$ and $\tilde{D}_c$ should minimize their dependency too. We thus minimize the MI of $\tilde{D}_c$ and $\tilde{A}_c$,

$$\mathcal{I}(\tilde{D}_c, \tilde{A}_c) = \mathcal{H}_{\tilde{D}_c} + \mathcal{H}_{\tilde{A}_c} - \mathcal{H}_{\hat{A}_c, \hat{D}_c} \qquad (25)$$

as a function of w_1 and w_2. Now, Eqs. (14,16) express pointwise mixture and separation processes: the airlight in a point is mixed only with the direct transmission of the same point in the raw frames. For pointwise [8] mixtures, Eq. (25) is equivalent to

$$\mathcal{I}(\tilde{D}_c, \tilde{A}_c) = \mathcal{H}_{\tilde{D}_c} + \mathcal{H}_{\tilde{A}_c} - \log|\det(\tilde{\mathbf{W}})| - \mathcal{H}_{I_c^{\max}, I_c^{\min}}. \qquad (26)$$

Here $\mathcal{H}_{I_c^{\max}, I_c^{\min}}$ is the joint entropy of raw frames. Its value is a constant set by the raw data, and hence does not depend on $\tilde{\mathbf{W}}$. For this reason, we ignore it in the optimization process. Moreover, note from Eq. (21), that $\tilde{A}_c$ does not depend on w_1, w_2. Therefore, $\mathcal{H}_{\tilde{A}_c}$ is constant and can also be ignored in the optimization process. Thus, the optimization problem we solve is simplified to

$$\min_{w_1, w_2} \left\{ \mathcal{H}_{\tilde{D}_c} - \log|w_2 + w_1| \right\} \ , \qquad (27)$$

where the $\log|w_2 + w_1|$ term expresses $\log|\det(\tilde{\mathbf{W}})|$ for the matrix given in Eq. (24).

3.4 Simplicity by a Probability Model

In this section, further simplifications are performed, allowing for more efficient optimization. Recall that to enable linear ICA, we use high spatial frequency bands. In natural scenes, sub-band images are known to be *sparse*. In other words, almost all the pixels in a sub-band image have values that are very close to zero. Hence, the probability density function (PDF) of a sub-band pixel value is sharply peaked at the origin. A PDF model that is widely used for such images is the generalized Laplacian (see for example [29])

$$\mathrm{PDF}(\tilde{D}_c) = c(\rho) \exp(-|\tilde{D}_c|^\rho) \ , \qquad (28)$$

where $\rho \in (0, 2)$ is a parameter of the distribution, and $c(\rho)$ is the normalization constant. Note that a general model should contain a scale parameter, associated with the standard deviation (STD) of the distribution. However, we do not need this scale parameter. The reason is that ICA recovers each signal up to an arbitrary intensity scale, as mentioned. Thus, optimizing a scale parameter during ICA is meaningless. We thus set a fixed unit scale to the PDF in Eq. (28). This means that whatever $\tilde{D}_c(x, y)$ is, its values

are *implicitly* re-scaled by the optimization process to fit this unit-scale model.

This prior of image statistics can be exploited for the entropy estimation needed in the optimization [1, 35]. Entropy is defined as (see for example [2])

$$\mathcal{H}_{\tilde{D}_c} = \mathcal{E}\left\{-\log[\text{PDF}(\tilde{D}_c)]\right\} , \qquad (29)$$

where $\mathcal{E}$ denoted expectation. Substituting Eq. (28) into Eq. (29) and replacing the expectation with empirical averaging, the entropy estimate is

$$\hat{\mathcal{H}}_{\tilde{D}_c} = C(\rho) + \frac{1}{N}\sum_{x,y}|\tilde{D}_c(x,y)|^\rho . \qquad (30)$$

Here N is the number of pixels in the image, while $C(\rho) = \log[c(\rho)]$. Note that $C(\rho)$ does not depend on $\tilde{D}_c$, and thus is independent of w_1 and w_2. Hence, $C(\rho)$ can be ignored in the optimization process. We can see that the generalized Laplacian model simplifies the optimization problem to

$$\min_{w_1,w_2}\left\{-\log|w_2 + w_1| + \frac{1}{N}\sum_{x,y}|\tilde{D}_c(x,y)|^\rho\right\} . \quad (31)$$

The cost function is a simple expression of the variables.

3.5 A Convex Formulation

Eq. (31) is simple enough to ease optimization. However, we prefer a convex formulation of the cost function, as it guarantees a unique solution, which can be reached efficiently using gradient methods.

First, we note that the term $[-\log|w_2 + w_1|]$ in Eq. (31) is a convex function of w_1 and w_2, in the problem domain. The reason is that by definition, $p \in [0,1]$, thus (see Eq. 23) it follows that $(w_2 + w_1) \in [0,2]$. In the non-negative domain, the $[-\log]$ function is convex. Moreover, $\tilde{D}_c(x,y)$ is a convex function of w_1 and w_2, as seen in the linear relation given in Eq. (22). Hence, the overall cost function (31) is convex, if $|\tilde{D}_c|^\rho$ is a convex function of $\tilde{D}_c$.

The desired situation of having $|\tilde{D}_c|^\rho$ convex occurs only if $\rho \geq 1$. Apparently, we should estimate ρ at each iteration of the optimization, by fitting the PDF model (28) to the values of $\tilde{D}_c(x,y)$. However we avoid this operation. Instead, we *set* the value of ρ to fit our purposes. Note that $\rho < 1$ for sparse signals as sub-band images. The PDF representing the sparsest signal that yields a convex function in Eq. (31) corresponds to $\rho = 1$. Thus we decided to use $\rho = 1$ (see also [1, 15, 28, 35]). By this decision, we may have sacrificed some accuracy, but enabled convexity.

In contrast to all the steps described in the previous sections, which were accurate, the use of $\rho = 1$ is an *approxi-*

mation. It turns the minimization of $\mathcal{I}(\hat{A}, \hat{D})$ to the following problem

$$\min_{w_1,w_2}\left\{-\log|w_2 + w_1| + \frac{1}{N}\sum_{x,y}|\tilde{D}_c(x,y)|\right\} , \quad (32)$$

where $\tilde{D}_c(x,y)$ is given in Eq. (22). Eq. (32) is the core of our optimization. It is unimodal and efficient. For convex functions as such, convergence speed is enhanced by use of local gradients.[7]

3.6 Back to Dehazing

The optimization described in Secs. 3.3, 3.4 and 3.5 yields an estimate for w_1 and w_2. Term these estimates as $\hat{w}_1$ and $\hat{w}_2$, respectively. We now use them to derive an estimate for p. Apparently, from Eq. (23), p is simply the average of $\hat{w}_1$ and $\hat{w}_2$. However, ICA yields $\hat{w}_1$ and $\hat{w}_2$ up to a global scale factor, which is unknown. Fortunately, the following estimator

$$\hat{p} = \frac{\hat{w}_1 + \hat{w}_2}{\hat{w}_2 - \hat{w}_1} \qquad (33)$$

is invariant to that scale. This process is repeated in each color channel.

Once $\hat{p}$ is derived, it is used for constructing **W** in Eq. (17). Then, Eq. (16) separates the airlight $\hat{A}$ and the direct transmission $\hat{D}$. This recovery is *not* performed on the sub-band images. Rather, it is performed on the raw image representation, as in prior sky-based dehazing methods.

We stress that in this scheme, we bypass all inherent ICA ambiguities: permutation, sign and scale. Those ambiguities do not affect us, because we essentially recover the scene using a *physics-based method*, not a pure signal processing ICA. ICA is only used for finding a parameter p, and it is done in a way (Eq. 33) that is scale invariant.

A Note about Channel Voting

In principle, the airlight DOP p should be independent of the wavelet channel c. However, in practice, the optimization described above yields, for each wavelet channel, a different estimated value $\hat{p}$. The reason is that some channels comply with the independence assumption of Sec. 3.1, while others do not. Nevertheless, there is a way to eliminate poor channels. Channels that do not obey the assumptions yield a random value for $\hat{p}$. On the other hand, channels that are "good" yield a consistent estimate. Hence the optimal $\hat{p}$ is determined by voting. Moreover, this voting is constrained to the range $\hat{p} \in [0,1]$, due to Eq. (32). Any value outside this range is ignored.

Let us describe an example. We acquired two frames via a polarizer, $I^{\max}$ and $I^{\min}$, using a Nikon D-100 camera,

---

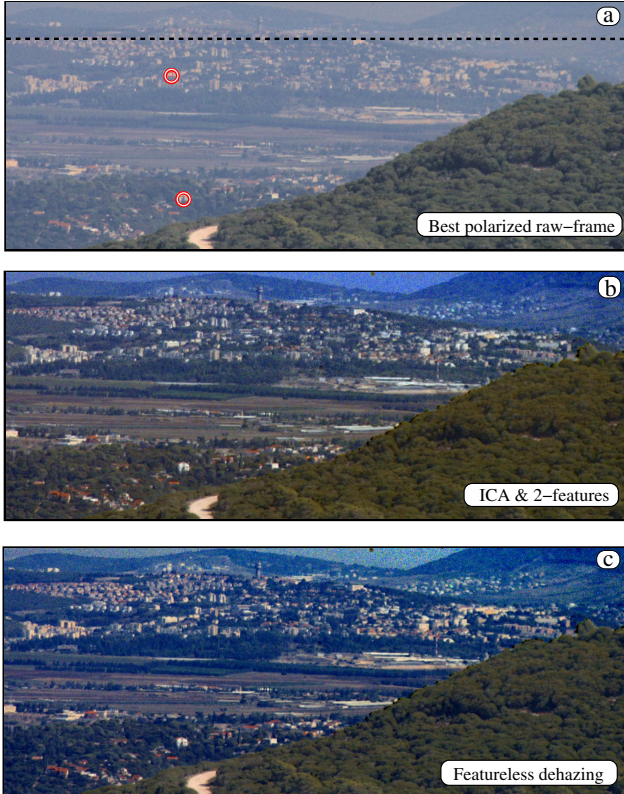[7]See [10] for the differentiation of the absolute value function.

Figure 3. Skyless dehazing of **Scene 1**. [a] Best polarized image. The parameters are estimated using the part of the image below the dashed line. The two circles mark buildings which are placed in different depths. [b] Dehazing using ICA and two features. [c] Featureless dehazing. **To observe the color effects, please view the paper on the computer monitor.**

having a linear radiometric response. The image $I^{\min}$ is shown[8] in Fig. 3a. To challenge the algorithm, we *cropped* the raw images, to remove all sky-areas from the FOV. In Fig. 3a, the section used for estimation is below the dashed line. Then, the process described in this section was performed. The process yielded a set of $\hat{p}$ values, one for each channel. Fig. 4 plots the voting result as a histogram per color channel. The dominant bar in each histogram determines the selected values of $\hat{p}$.

To assess the accuracy of this estimate, "ground truth" is needed. We obtain it by expanding the FOV of Fig. 3 beyond the dashed line, and measuring the DOP directly from the sky. This value, denoted p_{sky} is compared to $\hat{p}$ in Table. 1, under **Scene 1**. A result of another experiment done elsewhere is also shown in Table. 1, under **Scene 2**, corresponding to the data shown in Fig. 5. Clearly, p_{sky} and

---

[8]For clarity of display, the images shown in this paper have undergone the same standard luminance contrast stretching, while their chroma was untouched. This operation was done only towards the display. The algorithms described in the paper were run on raw, unstretched data.
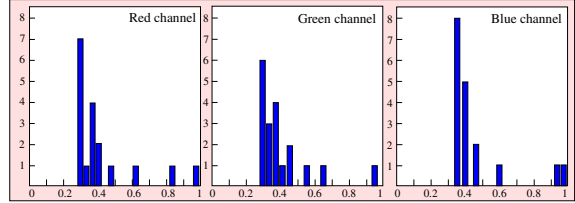

Figure 4. Histograms of $\hat{p}$ across the wavelet channels, corresponding to Fig. 3. In each color channel we choose the most frequent value of $\hat{p}$.

	Scene 1		**Scene 2**	
	$\hat{p}$	p_{sky}	$\hat{p}$	p_{sky}
Red	0.30	0.32	0.28	0.32
Green	0.33	0.34	0.32	0.34
Blue	0.36	0.36	0.36	0.36

Table 1. The result of the blind estimation of $\hat{p}$, compared with the value p_{sky}, which is measured from the sky. The two methods yield very close results.

$\hat{p}$ are very close. We repeated the experiment on several scenes and days with consistent results.

4 Estimating A_∞

To recover $\hat{L}^{\text{object}}$, there is a need to divide $\hat{D}$ by the estimated transmittance, to invert Eq. (1). Thus, $t(x, y)$ should be estimated. According to Eq. (11), this can be done using the (newly) estimated airlight $A(x, y)$. However, this step requires the knowledge of an additional parameter, A_∞, which was not derived in Sec. 3. This section describes ways to estimate A_∞, using I^{total} and the just derived $\hat{p}$ and $\hat{A}$.

4.1 Feature-Based Estimation

In this section we describe a method to estimate A_∞, based on identification of two similar features in the scene. Suppose we can mark two scene points (x_k, y_k), $k = 1, 2$, which, in the absence of scattering, would have a similar (unknown) radiance. For example, these can be two buildings which have an unknown radiance L^{build}. It is easy to show [25] from Eqs. (10,11,12) that

$$\hat{I}^{\text{total}}(k) = L^{\text{build}} + S^{\text{build}} \hat{A}(k) \ , \tag{34}$$

where $\hat{A}(k)$ is derived from Eqs. (10,33) and

$$S^{\text{build}} \equiv \left(1 - L^{\text{build}}/A_\infty\right) \tag{35}$$

is a constant.

Buildings at different distances have different intensity readouts, due to the effects of scattering. Therefore, they

Figure 5. Featureless dehazing of **Scene 2**. The parameters $\hat{p}$ and A_∞ were estimated using a cropped image reside below the dashed line

have different values of I^{total} and A. According to Eq. (34), $\hat{I}^{\text{total}}$ as a function of $\hat{A}$ forms a straight line. Such a line can be determined using two data points. Extrapolating the line, its intercept yields the estimated radiance value $\hat{L}^{\text{build}}$. Let the slope of the fitted line be S^{build}. We can now estimate A_∞ as

$$\hat{A}_\infty = \hat{L}^{\text{build}}/(1 - S^{\text{build}}) \ . \tag{36}$$

With $\hat{A}_\infty$, we can estimate t and compensate for it.

As an example, the two circles in Fig. 3a mark two buildings residing in different depths. The dehazed result is shown in Fig. 3b. For display, we show how the sky area is affected by this algorithm (although the sky area was not in use during calculations). Indeed, the haze is removed, and the colors are significantly recovered. We obtained such consistent results in many other experiments (see [22]).

4.2 Featureless Dehazing

It is possible to derive $\hat{A}_\infty$ in the following way. First, we roughly select a region in the FOV, that contains depth variations, yet with a similar underlying scene content across it. Then, we create a scatter plot of $\hat{A}$ vs. $\hat{I}^{\text{total}}$,
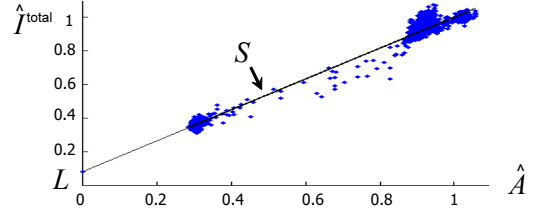

Figure 6. A scatter plot of $\hat{A}$ vs. $\hat{I}^{\text{total}}$, corresponding to a roughly selected area from Fig. 3.

as shown in Fig. 6. From a line fitted to this scatter plot, Eqs. (34,35,36) derive $\hat{A}_\infty$. Our experiments showed that $\hat{A}_\infty^{\text{blue}}$ is more accurate than the values of the other channels. Therefore, it is used to help determine the other channels as described in the following. We capitalize on an observation made by [18]: the orientation of the airlight color vector (in color space) is approximately invariant to distance. Indeed, this observation was consistent in every experiment we made. Let $\hat{A}^{\text{red}}(x, y)$, $\hat{A}^{\text{green}}(x, y)$ and $\hat{A}^{\text{blue}}(x, y)$ be the airlight values at the red, green and blue color channels, respectively, as derived by our ICA method. Define the ratios

$$r^{\text{red}}(x, y) = \frac{\hat{A}^{\text{red}}(x, y)}{\hat{A}^{\text{blue}}(x, y)} \ , \quad r^{\text{green}}(x, y) = \frac{\hat{A}^{\text{green}}(x, y)}{\hat{A}^{\text{blue}}(x, y)}. \tag{37}$$

According to [18], these ratios are approximately spatially invariant, hence their spatial mean

$$\bar{r}^{\text{red}} = \frac{1}{N} \sum_{x,y} r^{\text{red}}(x, y) \ , \quad \bar{r}^{\text{green}} = \frac{1}{N} \sum_{x,y} r^{\text{green}}(x, y) \tag{38}$$

indicates a relation between the sought color values of A_∞

$$\hat{A}_\infty^{\text{red}} = \bar{r}^{\text{red}} \hat{A}_\infty^{\text{blue}} \ , \quad \hat{A}_\infty^{\text{green}} = \bar{r}^{\text{green}} \hat{A}_\infty^{\text{blue}} \ . \tag{39}$$

Therefore $\hat{A}_\infty^{\text{blue}}$ indicates the rest of the channels.

Results of featureless dehazing are shown in Figs. 3c and 5. The colors of the dehazed images are nicely restored, (e.g, the red roofs) and the removed haze reveals many details, such as the background hills. It is preferable to automate this process. We now consider such an automation, based on optimization of the local image contrast.

5 Discussion

The core of this paper has been the blind estimation and separation of airlight. This was done in a mathematical method (ICA) that has solid foundations. It assumes that there are some image (frequency) components for which airlight is independent of the direct transmission, and that there are depth variations in the scene. Currently the compensation for the attenuation, as described in Sec. 4 is not

blind, but requires some user interaction. Thus, further work is needed to establish blind attenuation estimation. It is worth pursuing extensions of this work to other scattering modalities, such as underwater photography.

Acknowledgments

References

[1] P. Bofill and M. Zibulevsky. Underdetermined blind source separation using sparse representations. *Signal Processing*, 81:2353–62, 2001.

[2] T. M. Cover and J. A. Thomas. *Elements of Information Theory*. John Wiley and sons, NY, 1991.

[3] F. Cozman and E. Kroktov. Depth from scattering. In *Proc. IEEE CVPR*, pages 801–806, 1997.

[4] O. G. Cula, K. J. Dana, D. K. Pai, and D. Wang. Polarization multiplexing for bidirectional imaging. In *Proc. IEEE CVPR*, volume 2, pages 1116–1123, 2005.

[5] F. de la Torre, R. Gross, S. Baker, and B. V. K. Vijaya Kumar. Representational oriented component analysis (ROCA) for face recognition with one sample image per training class. In *Proc. CVPR*, volume 2, pages 266–273, 2005.

[6] H. Farid and E. H. Adelson. Separating reflections and lighting using independent components analysis. In *Proc. IEEE CVPR*, volume 1, pages 262–267, 1999.

[7] K. Garg and S. K. Nayar. Detection and removal of rain from videos. In *Proc. IEEE CVPR*, volume 1, pages 528–535, 2004.

[8] A. Hyvärinen, J. Karhunen, and E. Oja. *Independent component analysis*. John Wiley and Sons, NY, 2001.

[9] J. S. Jaffe. Computer modelling and the design of optimal underwater imaging systems. *IEEE J. Oceanic Eng.*, 15:101–111, 1990.

[10] P. Kisilev, M. Zibulevsky, and Y. Y. Zeevi. Multiscale framework for blind source separation. *J. of Machine Learning Research*, 4:1339–63, 2004.

[11] D. M. Kocak and F. M. Caimi. The current art of underwater imaging with a glimpse of the past. *MTS Journal*, 39:5–26, 2005.

[12] N. S. Kopeika. *A System Engineering Approach to Imaging*, pages 446–452. Bellingham, Wash: SPIE, 1998.

[13] T.-W. Lee and M. Lewicki. Unsupervised classification, segmentation, de-noising of images using ica mixture models. *IEEE Trans. IP*, 11:270 – 279, 2002.

[14] M. Levoy, B. Chen, V. Vaish, M. Horowitz, I. McDowall, and M. Bolas. Synthetic aperture confocal imaging. *ACM Trans. Graphics*, 23:825–834, 2004.

[15] Y. Li, A. Cichocki, and S. Amari. Analysis of sparse representation and blind source separation. *Neural Computation*, 16:1193–1234, 2004.

[16] D. Miyazaki and K. Ikeuchi. Inverse polarization raytracing: estimating surface shape of transparent objects. In *Proc. IEEE CVPR*, volume 2, pages 910–917, 2005.

[17] E. Namer and Y. Y. Schechner. Advanced visibility improvement based on polarization filtered images. In *Proc. SPIE 5888*, pages 36–45, 2005.

[18] S. G. Narasimhan and S. K. Nayar. Vision and the atmosphere. *Int. J. Comp. Vis.*, 48:233–254, 2002.

[19] D. Nuzilland, S. Curila, and M. Curila. Blind separation in low frequencies using wavelet analysis, application to artificial vision. In *Proc. ICA*, pages 77–82, 2003.

[20] J. P. Oakley and B. L. Satherley. Improving image quality in poor visibility conditions using a physical model for contrast degradation. *IEEE Trans. IP*, 78:167–179, 1998.

[21] B. Sarel and M. Irani. Separating transparent layers through layer information exchange. In *Proc. ECCV*, pages 328–341, 2004.

[22] Y. Y. Schechner. Home page: $www.ee.technion.ac.il/{\sim}yoav/$BlindDehazing/.

[23] Y. Y. Schechner and N. Karpel. Clear underwater vision. In *Proc. IEEE CVPR*, volume 1, pages 536–543, 2004.

[24] Y. Y. Schechner and N. Karpel. Recovery of underwater visibility and structure by polarization analysis. *IEEE J. Oceanic Eng.*, 30:570–587, 2005.

[25] Y. Y. Schechner, S. G. Narasimhan, and S. K. Nayar. Polarization-based vision through haze. *App. Opt.*, 42:511–525, 2003.

[26] Y. Y. Schechner, J. Shamir, and N. Kiryati. Polarization and statistical analysis of scenes containing a semi-reflector. *J. Opt. Soc. Amer. A*, 17:276–284, 2000.

[27] S. Shwartz, M. Zibulevsky, and Y. Y. Schechner. Fast kernel entropy estimation and optimization. *Signal Processing*, 85:1045–1058, 2005.

[28] S. Shwartz, M. Zibulevsky, and Y. Y. Schechner. Efficient separation of convolutive image mixtures. In *Proc. Int. Conf. on ICA and BSS (LNCS 3889)*, pages 246–253, 2006.

[29] E. P. Simoncelli. Statistical models for images: Compression, restoration and synthesis. In *Proc. IEEE Asilomar Conf. Sig. Sys. and Computers*, pages 673–678, 1997.

[30] J. Sun, J. Jia, C. K. Tang, and H. Y. Shum. Poisson matting. *ACM Trans. Graphics*, 23:315–321, 2004.

[31] T. Treibitz and Y. Y. Schechner. Instant 3Descatter. In *Proc. IEEE CVPR*, 2006.

[32] S. Umeyama and G. Godin. Separation of diffuse and specular components of surface reflection by use of polarization and statistical analysis of images. *IEEE Trans. PAMI*, 26:639–647, 2004.

[33] M. A. O. Vasilescu and D. Terzopoulos. Multilinear independent components analysis. In *Proc. IEEE CVPR*, volume 1, pages 547–553, 2005.

[34] L. B. Wolff. Polarization vision: a new sensory approach to image understanding. *Image & Vis. Comp.*, 15:81–93, 1997.

[35] M. Zibulevsky and B. A. Pearlmutter. Blind source separation by sparse decomposition in a signal dictionary. *Neural Computations*, 13:863–882, 2001.